

# Synthesis and Structure of an Ion-Exchanged SrTiO<sub>3</sub> Photocatalyst with Improved Reactivity for Hydrogen Evolution

Mingyi Zhang, Eric M. Lopato, Nnamdi N. Ene, Stephen D. Funni, Tianxiang Du, Kunyao Jiang, Stefan Bernhard, Paul A. Salvador, and Gregory S. Rohrer\*

BaTiO<sub>3</sub> heated in an excess of SrCl<sub>2</sub> at 1150 °C converts to SrTiO<sub>3</sub> through an ion exchange reaction. The SrTiO<sub>3</sub> synthesized by ion exchange produces hydrogen from pH 7 water at a rate more than twice that of conventional SrTiO<sub>3</sub> treated identically. The apparent quantum yield for hydrogen production in pure water of the ion exchanged SrTiO<sub>3</sub> is 11.4% under 380 nm illumination. The catalyst resulting from ion-exchange differs from conventional SrTiO<sub>3</sub> by having ≈2% residual Ba, inhomogeneous Cl-doping at a concentration less than 1%, Kirkendall voids in the centers of particles that result from the unequal rates of Sr and Ba diffusion together with the transport of Ti and O, and nanoscale regions near the surface that have lattice spacings consistent with the Sr-excess phase Sr<sub>2</sub>TiO<sub>4</sub>. The increased photochemical efficiency of this nonequilibrium structure is most likely related to the Sr-excess, which is known to compensate donor defects that can act as charge traps and recombination centers.

reactions.<sup>[4]</sup> This has motivated attempts to develop photocatalysts with enhanced charge-separation properties using defect engineering,<sup>[5,6]</sup> facet engineering,<sup>[7–9]</sup> and the construction of heterojunctions.<sup>[10–12]</sup> Recently, molten salt treatments have been used for synthesis and to optimize photocatalyst properties.<sup>[13,14]</sup> In a molten salt, the mass transfer between precursors is accelerated and, compared with conventional solid-state synthesis, lower reaction temperatures can be used.<sup>[15,16]</sup>

Al-doped SrTiO<sub>3</sub> is one of the most efficient particulate semiconductor-based photocatalysts that have been developed so far.<sup>[17]</sup> By selectively photodepositing cocatalysts on (100) and (110) facets, Domen and co-workers<sup>[18]</sup> reported an Al-doped SrTiO<sub>3</sub> catalyst with an external quantum efficiency for overall water splitting of

up to 96% at 360 nm. One step in the synthesis of this catalyst is heating in the presence of molten SrCl<sub>2</sub> in an alumina crucible. During this process, a small amount of Al from the crucible (≈1%) is dissolved into the SrTiO<sub>3</sub>. The process has also been reported to enhance the crystallinity of the SrTiO<sub>3</sub>.<sup>[19]</sup> While there is convincing physical evidence for the Al-doping, the support for the assertion that molten SrCl<sub>2</sub> improves the crystallinity of SrTiO<sub>3</sub> is not strong. It has more recently been reported that when SrTiO<sub>3</sub> particles with controlled shapes are heated in molten SrCl<sub>2</sub>, the shapes are preserved.<sup>[20]</sup> This suggests that, while some particle erosion or coarsening is possible, the particles do not completely dissolve and recrystallize.

While exploring the effects of molten salts on potential transition metal oxide photocatalysts, we found that when BaTiO<sub>3</sub> is heated in an excess of SrCl<sub>2</sub>, it is converted to SrTiO<sub>3</sub> through an ion exchange reaction. Driven by the large concentration gradient, Sr<sup>2+</sup> cations from the molten salt diffuse into the oxides and exchange with Ba<sup>2+</sup>, and Kirkendall cavities form at the center of particles due to the unequal diffusion rates between Sr<sup>2+</sup> and Ba<sup>2+</sup>. The resulting SrTiO<sub>3</sub> exhibits a remarkable photocatalytic performance and produces hydrogen from pure water at a rate two times higher than conventional SrTiO<sub>3</sub> that has not undergone ion exchange. The improved reactivity is most likely related to the formation of metastable Ruddlesden–Popper Sr<sub>2</sub>TiO<sub>4</sub> thin layers in the near surface region, observed by high-resolution transmission electron microscopy


## 1. Introduction

Photocatalytic water splitting, a reaction that can directly convert water into hydrogen and oxygen under illumination, has attracted significant attention in past decades.<sup>[1,2]</sup> At present, two of the major issues that limit its application are the rapid recombination of photogenerated charge carriers<sup>[3]</sup> and surface back

M. Zhang, N. N. Ene, S. D. Funni, T. Du, K. Jiang, P. A. Salvador, G. S. Rohrer

Department of Materials Science and Engineering  
Carnegie Mellon University  
5000 Forbes Ave, Pittsburgh, PA 15213, USA  
E-mail: gr20@andrew.cmu.edu

E. M. Lopato, S. Bernhard  
Department of Chemistry  
Carnegie Mellon University  
4400 Fifth Ave, Pittsburgh, PA 15213, USA

 The ORCID identification number(s) for the author(s) of this article can be found under <https://doi.org/10.1002/admi.202202476>.

© 2023 The Authors. Advanced Materials Interfaces published by Wiley-VCH GmbH. This is an open access article under the terms of the Creative Commons Attribution License, which permits use, distribution and reproduction in any medium, provided the original work is properly cited.

DOI: 10.1002/admi.202202476

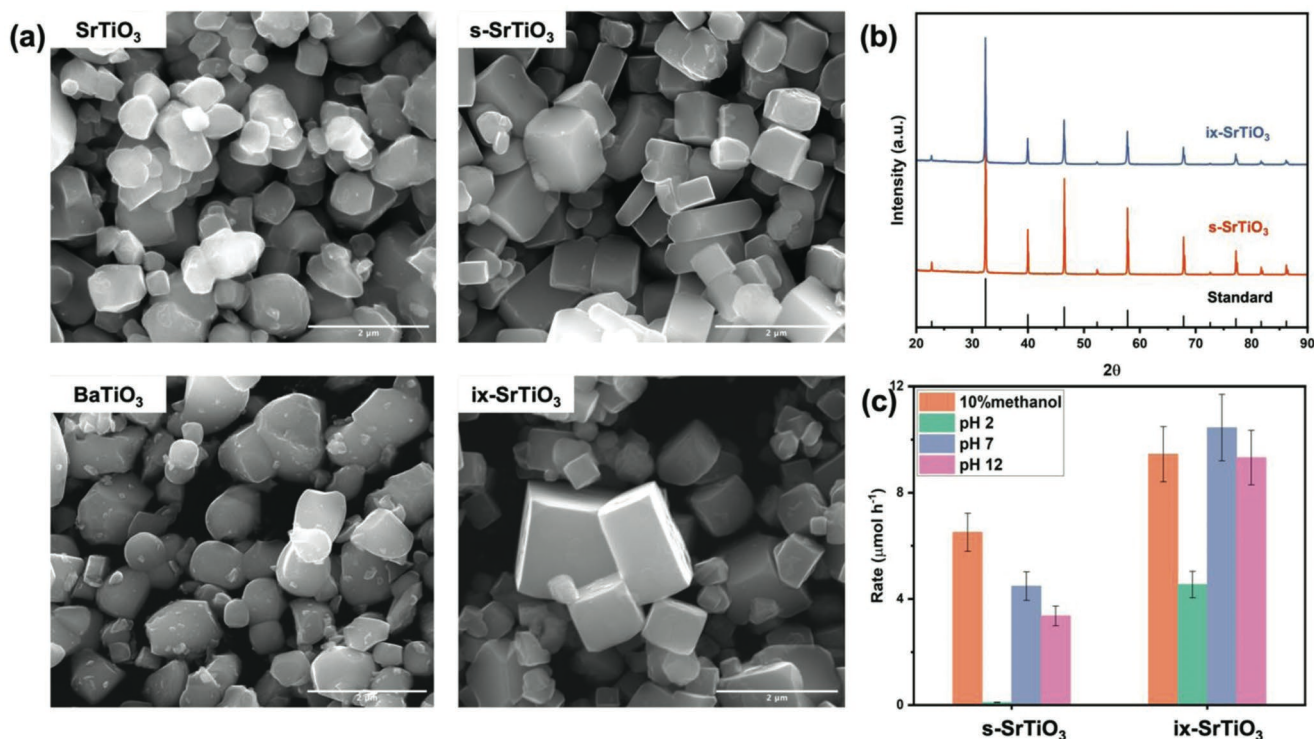
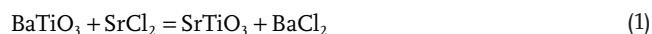


**Figure 1.** SEM images of: a) pristine SrTiO<sub>3</sub>, pristine BaTiO<sub>3</sub>, s-SrTiO<sub>3</sub> (SrTiO<sub>3</sub> that has undergone a molten SrCl<sub>2</sub> treatment), and ix-SrTiO<sub>3</sub> (BaTiO<sub>3</sub> that has undergone a molten SrCl<sub>2</sub> treatment). Scale bar: 2 μm. b) XRD patterns of the two samples with a standard SrTiO<sub>3</sub> pattern plotted as black droplines (ICDD: 01-074-1296). c) Mean photocatalytic maximum H<sub>2</sub> production rates (each determined from six samples) in 10% methanol solution, pH 2 water, pH 7 water, and pH 12 water under 380 nm illumination. The bars represent standard deviations.

(TEM) because Sr-excess is known to compensate recombination centers. The observations demonstrate that ion exchange reactions make it possible to synthesize photocatalysts with structures not accessible by conventional approaches.

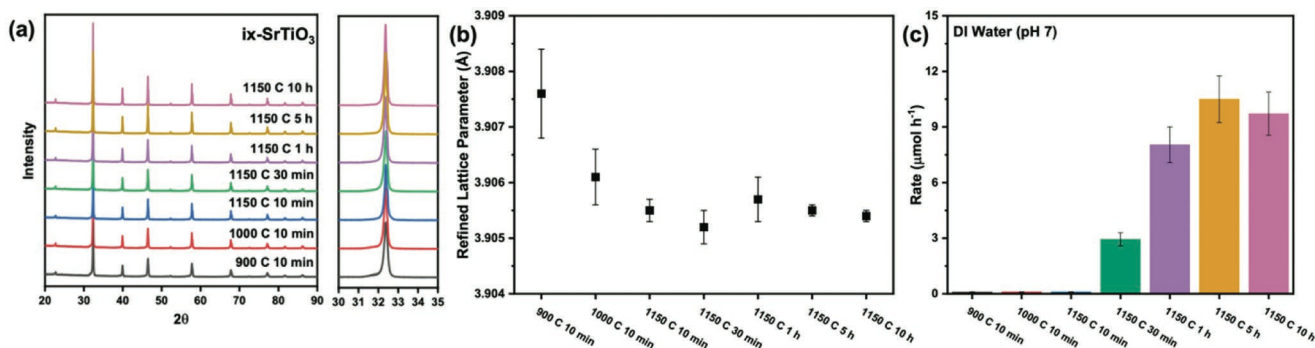
## 2. Results and Discussion

Figure 1a compares the secondary electron microscope (SEM) images of SrTiO<sub>3</sub> and BaTiO<sub>3</sub> before and after being heated at 1150 °C for 10 h in a ten times excess of molten SrCl<sub>2</sub> in an alumina crucible. The X-ray diffraction (XRD) patterns of the resulted powders are presented in Figure 1b. Based on the diffraction patterns and refined lattice parameters (Table S1, Supporting Information), BaTiO<sub>3</sub> has converted to SrTiO<sub>3</sub>. The ion-exchanged SrTiO<sub>3</sub> derived from BaTiO<sub>3</sub> will be referred to as ix-SrTiO<sub>3</sub> throughout the remainder of this paper. The equilibrium constant for the reaction:



is greater than 1 at 1150 °C (with a free energy change of  $-45.47 \text{ kJ mol}^{-1}$  in the standard condition), so it should not be surprising that SrTiO<sub>3</sub> forms under these conditions. This is analogous to ion exchange reactions recently reported by O'Donnell et al.<sup>[21]</sup> Pristine SrTiO<sub>3</sub> without any treatment and SrTiO<sub>3</sub> that has been heated in molten SrCl<sub>2</sub> using the same conditions as the BaTiO<sub>3</sub> ion exchange reaction will be referred to as SrTiO<sub>3</sub> and s-SrTiO<sub>3</sub>, respectively.

The s-SrTiO<sub>3</sub> and ix-SrTiO<sub>3</sub> (both treated in molten SrCl<sub>2</sub> in the same conditions) were loaded with a 0.1 wt% Rh-Cr-O cocatalyst and the rate of hydrogen production was measured using a parallelized and automated photochemical reactor (PAPCR).<sup>[22]</sup> The Rh-Cr-O cocatalyst serves as electron accumulation sites and is kinetically active for charge transfer to H<sup>+</sup>/H<sub>2</sub> redox couples, and the O<sub>2</sub>/H<sub>2</sub>O anodic half reaction is supposed to take place on the SrTiO<sub>3</sub> surfaces.<sup>[23]</sup> The catalysts were in DI water whose pH was adjusted to pH 2, 7, or 12, or in a 10% methanol solution with unadjusted pH. Photoreactions were stimulated by 380 nm light from two LED chips. The results, shown in Figure 1c, clearly show that the ix-SrTiO<sub>3</sub> produced more hydrogen than the conventional s-SrTiO<sub>3</sub> under all conditions tested. The ix-SrTiO<sub>3</sub> sample in pH 7 water produced hydrogen at the greatest rate (10 μmol h<sup>-1</sup>), which is more than twice the rate of hydrogen production from the conventional s-SrTiO<sub>3</sub> (4 μmol h<sup>-1</sup>). The apparent quantum yield (AQY) of ix-SrTiO<sub>3</sub> was determined using a larger reactor with a more well-defined illumination geometry described in the Experimental Section and Figure S1 (Supporting Information) and found to be 11.4% in 380 nm light. Note that the highest measured AQY at 380 nm SrTiO<sub>3</sub> is 33.6%, but these particles had controlled shapes with two different cocatalysts selectively deposited on different facets of each crystal.<sup>[18]</sup> Both s-SrTiO<sub>3</sub> and ix-SrTiO<sub>3</sub> produce hydrogen at a higher rate at pH 7 than that at pH 2 and 12, which is consistent with our previous work reported for undoped SrTiO<sub>3</sub> single crystals<sup>[24]</sup> and Al-doped SrTiO<sub>3</sub> particles.<sup>[20]</sup> This is because the amount of surface charge influences band bending,



**Figure 2.** a) XRD patterns of BaTiO<sub>3</sub> treated in the molten SrCl<sub>2</sub> for a variety of temperature and time combinations. b) Lattice parameters refined from the XRD patterns. c) Photocatalytic H<sub>2</sub> production rates of the samples in pH 7 DI water. The bars represent standard deviations from six distinct measurements.

and pH 7 corresponds to a surface charge where neither the photocathodic nor the photoanodic reaction limit the overall reaction rate. For ix-SrTiO<sub>3</sub>, the rate is higher in pH 7 water than that in 10% methanol solutions, indicating that the anodic half reaction is no longer the rate-limiting reaction. To check the photostability, the same samples have been tested for another run under the same conditions, and the hydrogen evolution data are shown in Figure S2 (Supporting Information), indicating that the catalysts are stable after at least 30 h of illumination.

To better understand the reaction that forms ix-SrTiO<sub>3</sub> and its effect on the reactivity, the BaTiO<sub>3</sub> precursor was exposed to molten SrCl<sub>2</sub> at different temperatures for different times, with the mildest conditions being 10 min at 900 °C. The XRD patterns and SEM images from these materials are shown in Figure 2a and Figure S3 (Supporting Information), respectively. Note that in all conditions, the patterns indexed are cubic, meaning that the critical concentration of Sr needed to convert the solid solution to a cubic phase ( $x = 0.23$  in Sr<sub>x</sub>Ba<sub>1-x</sub>TiO<sub>3</sub>)<sup>[25]</sup> occurred within 10 min at 900 °C. However, the refined lattice parameters (see Figure 2b) indicated that the samples heated at 900 and 1000 °C did not complete the conversion to SrTiO<sub>3</sub> in 10 min. Evidence for the incomplete and probably inhomogeneous reaction is found in the tail of the (110) diffraction peak. The tail to smaller 2θ angles arises from regions of the crystals richer in Ba that have a larger lattice spacing. These annealing conditions, which did not result in a complete conversion to SrTiO<sub>3</sub>, impacted the rate of hydrogen production in pH 7 water (see Figure 2c). The samples heated at 900 and 1000 °C did not produce hydrogen at a rate detectable by the PAPCR. However, all ix-SrTiO<sub>3</sub> samples heated at 1150 °C produced measurable rates of hydrogen, with the samples heated for 5 and 10 h having the highest and similar rates of hydrogen production, suggesting that no significant composition changes occur with additional annealing at 5 h. Note that the molten SrCl<sub>2</sub> treatment also modifies the SrTiO<sub>3</sub> surface and improves the reactivity; the poor reactivities at 10 and 30 min suggest that the surface modification is incomplete at such a short time, although the ion exchange is nearly complete.

The bulk composition was studied with inductively coupled plasma - optical emission spectrometry (ICP-OES) analysis and the results are shown in Table S2 (Supporting Information). Both s-SrTiO<sub>3</sub> and ix-SrTiO<sub>3</sub> have small but detectable amounts of Al. Approximately 2% Ba was detected in the ix-SrTiO<sub>3</sub>,

indicating the ion exchange reaction is nearly complete. To determine if Cl exchanged into the samples while exposed to SrCl<sub>2</sub>, we used X-ray fluorescence (see Table S2, Supporting Information). Both samples contained a small amount of Cl, which likely substitutes on an O site. The ix-SrTiO<sub>3</sub> sample has a greater Cl concentration than the conventional s-SrTiO<sub>3</sub> sample. It is possible that the lattice expansion from the larger Ba ions makes it possible for more Cl to diffuse into the crystal. To examine the surface composition, X-ray photoelectron spectroscopy (XPS) experiments were conducted, and the results are shown in Figures S4–S5 and Table S3 (Supporting Information). While both samples treated in molten SrCl<sub>2</sub> have similar surface compositions, they are quite different from the untreated SrTiO<sub>3</sub> sample, having more surface hydroxyls and a greater Sr/Ti ratio. The specific surface areas of both s-SrTiO<sub>3</sub> and ix-SrTiO<sub>3</sub> have been measured and presented in Table S2 and Figure S6 (Supporting Information), suggesting that the two materials have similar surface areas and reaction sites.

To determine if there were composition gradients within the crystal, we used a focused ion beam (FIB) to cut into the middle of the sample and energy dispersive spectroscopy (EDS) to map the composition (see Figure 3). To make it easier to interpret the SEM, a schematic illustration of the FIB experiment is shown in Figure 3a. As shown in Figure 3b, upon cutting the particles, it became apparent that the ix-SrTiO<sub>3</sub> particles had internal cavities (labeled with arrows), while the conventional s-SrTiO<sub>3</sub> did not (see Figure S7, Supporting Information). These cavities likely form as a result of the well-known Kirkendall effect.<sup>[26]</sup> If Ba diffuses out of the crystal faster than Sr diffuses in, then internal cavities can form, as long as it is also possible to diffuse Ti and O away from the center of the crystal. Based on UV–vis diffuse reflectance (Figure S8, Supporting Information), these pores have no detectable effect on the optical absorption of the particles. To investigate the possibility that there was a gradient in the distribution of remaining minority components (Ba, Al, Cl), we used EDS mapping on the internal surface exposed by the FIB, as shown in Figure 3c. The elemental maps of the majority components (Sr, Ti, O) have a nearly uniform gradient from the upper left to the lower right, because the particle becomes thinner until it ends in the lower right-hand corner. The distributions of Ba and Al do not differ enough from the majority elements to clearly indicate a gradient. The Cl, on the other hand, appears to have a concentration maximum near

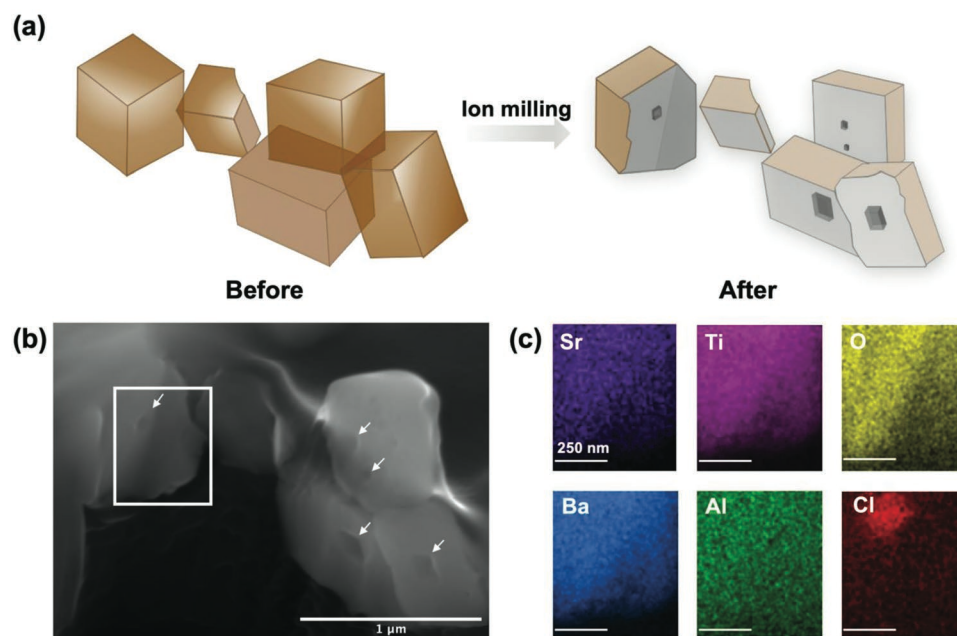


**Figure 3.** a) Schematic illustration of the preparation of ix-SrTiO<sub>3</sub> particle cross-section samples via ion milling. b) SEM images of ix-SrTiO<sub>3</sub> particle cross-section samples prepared via FIB milling. c) EDS element maps of the box region in (b).

the center of the particle. The presence of a Cl gradient is consistent with the XRF and XPS results; XPS, which is surface sensitive, detects no Cl (see Figure S5, Supporting Information), while XRF, which is sensitive to deeper regions within the crystal, does detect Cl.

The Kirkendall voids and the inhomogeneous Cl distribution result from kinetic limitations in the ion exchange reaction. Based on the conclusion that Sr diffuses inward more slowly than Ba diffuses out, it is possible that the surface region is enriched in Sr. While there was no obvious Sr enrichment in the EDS maps, particles were also examined by much higher-resolution TEM (see Figure 4). In the high-resolution image (see Figure 4a), the spacing between the lattice fringes in the very outer region is measured to be 0.175 nm, consistent with the spacing of the {120} planes of SrTiO<sub>3</sub>. The selected area diffraction pattern (see Figure 4b) confirms that the image is near the [120] zone axis. Below this, there are additional lattice fringes with twice the spacing. This is a lattice spacing not found in SrTiO<sub>3</sub>; it is also noteworthy that the lattice fringes with the wider spacing are misoriented by  $\approx 2^\circ$  from the SrTiO<sub>3</sub> {120} planes. As illustrated in Figure 4c, this doubled period and small inclination angle are consistent with the {102} planes of Sr<sub>2</sub>TiO<sub>4</sub>, if it were epitaxially oriented on SrTiO<sub>3</sub> such that both the [100] and [001] axes of both structures were aligned. Sr<sub>2</sub>TiO<sub>4</sub> is referred to as a Ruddlesden–Popper phase and adopts the K<sub>2</sub>NiF<sub>4</sub> structure.<sup>[27]</sup> Using the ideal lattice parameters, the misorientation between {120}<sub>p</sub> and {102}<sub>rp</sub> should be 3.5°, where the subscripts p and rp denote the perovskite and Ruddlesden–Popper structure, respectively.

The observation of one set of lattice fringes is not sufficient for phase identification with certainty. However, Sr<sub>2</sub>TiO<sub>4</sub> is known to form from SrTiO<sub>3</sub> in SrO-rich conditions and grow epitaxially on SrTiO<sub>3</sub> with this orientation relationship,<sup>[28]</sup> so this is a plausible explanation for the contrast in the TEM

images. Note that the diffraction pattern in Figure 4b is formed from the entire field of view of Figure 4a and does not have spots corresponding to the larger lattice spacing. If the aperture is reduced to include only the area with the larger interplanar spacing, there is not enough intensity to form a pattern, consistent with the absence of spots in the pattern from the larger field of view. In an ideal case, we would collect images and diffraction patterns from a combination of low index orientations, but here we are constrained to studying only small intergrowths in the electron transparent edges of irregularly oriented crystals. Given these constraints, a likely interpretation of the larger interplanar spacing is that there are small intergrowths of the Sr-rich phase, Sr<sub>2</sub>TiO<sub>4</sub> near the SrTiO<sub>3</sub> surface.

Schematics illustrating the differences between s-SrTiO<sub>3</sub> and ix-SrTiO<sub>3</sub> are presented in Figure 5. Among these differences, the residual Ba, Kirkendall voids, and Cl impurities seem unlikely to have a significant effect on the reactivity. The residual Ba, for example, is an isovalent impurity on the A-site and is not electrically active. Furthermore, the similarity of the bandgaps of SrTiO<sub>3</sub> and BaTiO<sub>3</sub> suggests that a small amount of Ba will not influence the absorption edges.<sup>[29]</sup> This is verified by the fact that the diffuse reflectance spectra of ix-SrTiO<sub>3</sub> and conventional s-SrTiO<sub>3</sub> are indistinguishable. One might hypothesize that the Kirkendall voids increase light scattering in a way that increases absorption, but this was also not evident in the diffuse reflectance spectra. Finally, Cl substituted on an O site (Cl<sub>o</sub><sup>•</sup>) has a positive effective charge and this has the potential to influence the reactivity, but it is also present in the s-SrTiO<sub>3</sub>. If the ix-SrTiO<sub>3</sub> has more Cl<sub>o</sub><sup>•</sup> in the center of the particle, as indicated by the EDS mapping, then the core might be relatively positively charged with respect to the surface and this would encourage the transport of photogenerated holes to the surface, promoting the oxidation reaction that is usually thought to be rate limiting.<sup>[30,31]</sup> However, the electrical char-

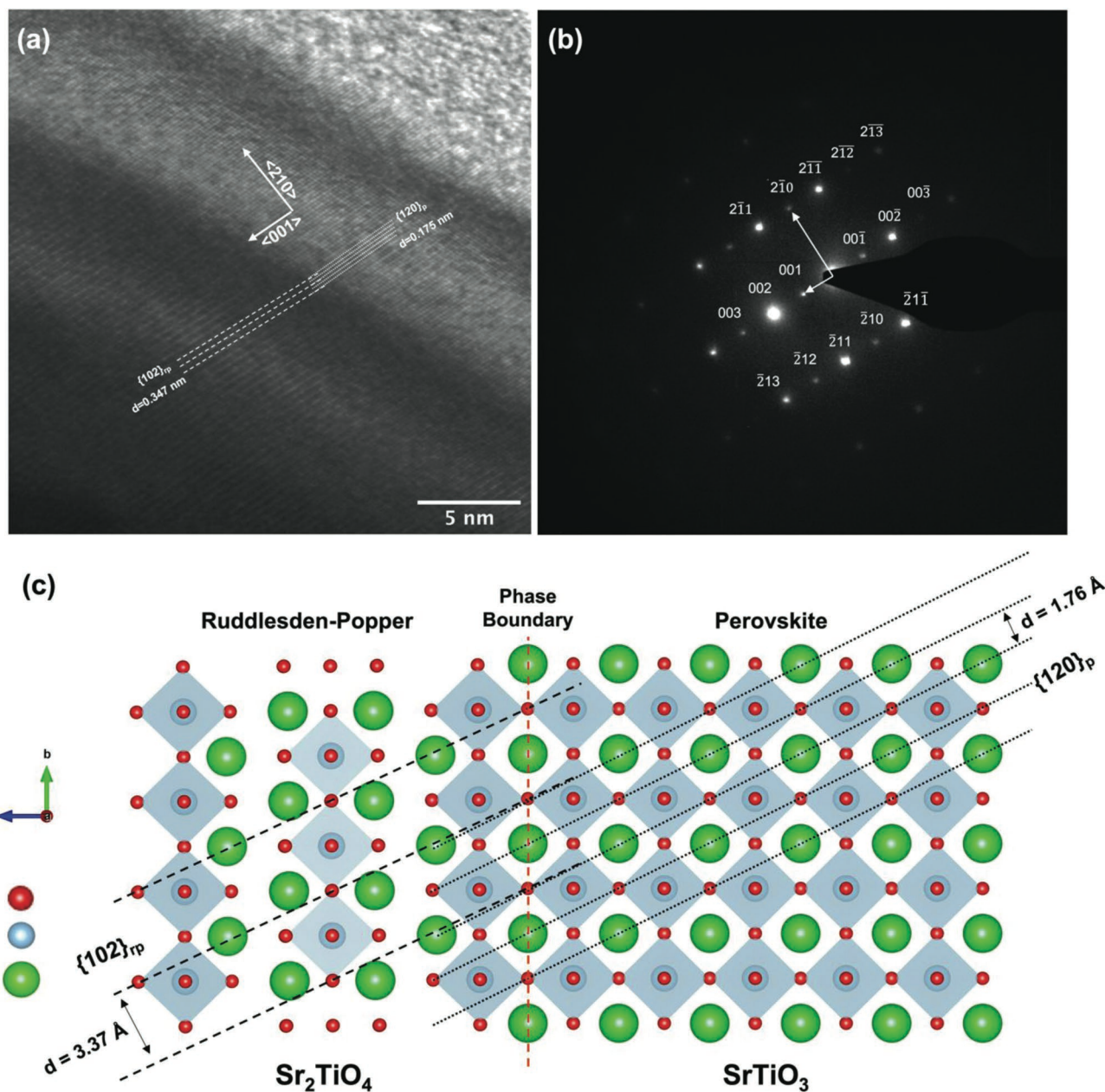


**Figure 4.** a) High-resolution TEM image of a particle edge of ix-SrTiO<sub>3</sub>. b) SAED pattern recorded from the lattice in (a). A schematic illustration of the structure in (a) is shown in: c). Note that this schematic is constructed assuming that Sr<sub>2</sub>TiO<sub>4</sub> has the same lattice constant for the a-lattice as SrTiO<sub>3</sub> ( $a_{\text{Sr}_2\text{TiO}_4} = a_{\text{SrTiO}_3}$ ).

acteristics of this impurity are similar to that of the dominant point defect in SrTiO<sub>3</sub>, the O vacancy ( $V_{\text{O}}^{\bullet}$ ), and these defects with positive effective charge are compensated by substitutional Al ( $Al'_{\text{Ti}}$ ) according to the electroneutrality condition  $[Al'_{\text{Ti}}] = 2[V_{\text{O}}^{\bullet}] + [Cl_{\text{O}}^{\bullet}]$ . Therefore, the effect of substitutional Cl on the reactivity is less clear.

Based on past work, the Sr-excess phase in the near surface region seems more likely to be responsible for the increased photocatalytic reactivity.<sup>[32–34]</sup> For example, Kato et al.<sup>[33]</sup> reported that SrTiO<sub>3</sub> with excess Sr obtains the highest water-splitting activity. More recently, Vijay et al.<sup>[34]</sup> have compared the photocatalytic reactivity of SrTiO<sub>3</sub>, Sr<sub>2</sub>TiO<sub>4</sub>, and Sr<sub>3</sub>Ti<sub>2</sub>O<sub>7</sub>

and found that both Sr-rich compounds evolved more hydrogen than SrTiO<sub>3</sub>. While the mechanism by which excess Sr leads to improved reactivity is not entirely clear, Yamada et al.<sup>[32]</sup> have shown that as the Sr/Ti ratio increases, charge carrier trapping decreases, and they associated this with an increase in the rate of water splitting. Moreover, charge separation could occur at the phase boundary between SrTiO<sub>3</sub> and Sr<sub>2</sub>TiO<sub>4</sub>. Based on the DFT calculations by Bilc et al.,<sup>[35]</sup> the valance band edge of Sr<sub>2</sub>TiO<sub>4</sub> is about 0.3 eV higher than SrTiO<sub>3</sub> along the [001] direction; this can promote the migration of photogenerated holes to the surface. The construction of such heterojunction is known to contribute to the overall reactivity.<sup>[36,37]</sup> A schematic

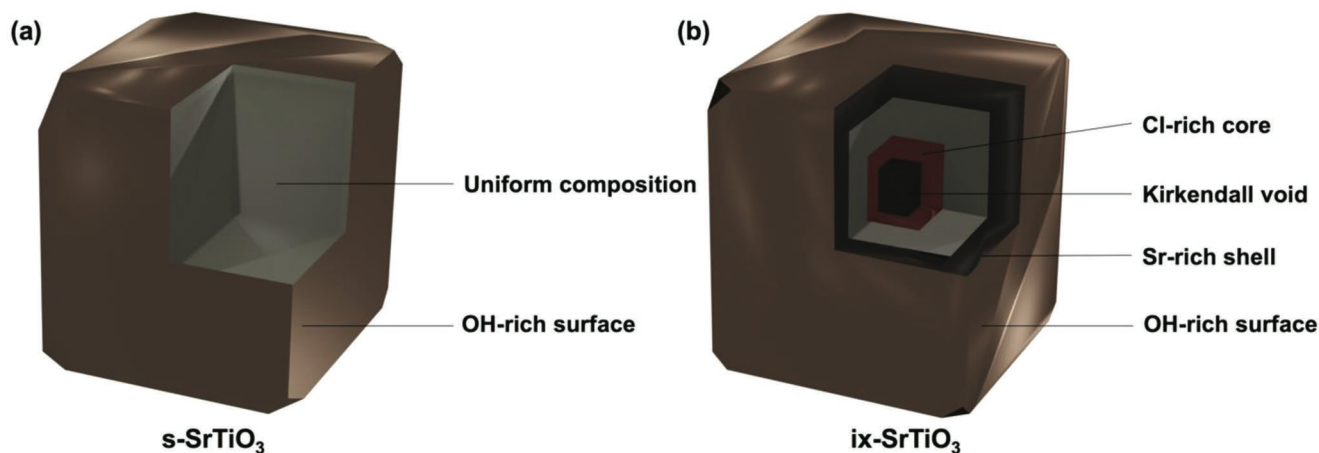
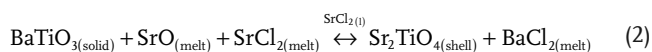


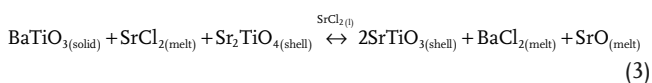
**Figure 5.** Schematic illustrations of: a) s-SrTiO<sub>3</sub> and b) ix-SrTiO<sub>3</sub>.

of the possible charge separation process is illustrated in Figure S9 (Supporting Information).

The observation of Kirkendall voids and the formation of single-phase solid solutions in the incomplete reactions carried out for shorter durations at lower temperatures suggest that the reaction occurs by ion-exchange rather than a reconstructive mechanism. However, the existence of Sr<sub>2</sub>TiO<sub>4</sub> in the near surface region indicates that the conversion of BaTiO<sub>3</sub> to SrTiO<sub>3</sub> is not an ideal topotactic reaction. For example, the formation of Kirkendall voids indicates not only that Sr diffuses into the crystal more slowly than Ba diffuses out but also that Ti and O must diffuse out of the void region. The formation of Sr<sub>2</sub>TiO<sub>4</sub> suggests Sr-rich conditions and this is not surprising for a SrCl<sub>2</sub> melt in ambient atmosphere, where SrO will be available.<sup>[38]</sup> As part of the ion exchange, Sr is migrating into the crystal and under conditions of excess SrO and one can imagine Sr<sub>2</sub>TiO<sub>4</sub> is formed by the following reaction:



Because the equilibrium state is presumably the complete conversion to SrTiO<sub>3</sub> (assuming a sufficient Sr reservoir), the outward diffusion of Ti and O can convert Sr<sub>2</sub>TiO<sub>4</sub> back to SrTiO<sub>3</sub>, consistent with Kirkendall void formation and an overall free energy reduction:



The observation of thin layers of Sr<sub>2</sub>TiO<sub>4</sub> in the TEM image suggests that some of the Sr<sub>2</sub>TiO<sub>4</sub> formed by reaction 2 is kinetically trapped near the surface during the ion exchange process.

### 3. Conclusion

In summary, ix-SrTiO<sub>3</sub>, produced by ion exchange from BaTiO<sub>3</sub> in a SrCl<sub>2</sub> melt, produces hydrogen at a rate more than twice that of conventionally synthesized s-SrTiO<sub>3</sub> photocatalysts. Among the difference between ix-SrTiO<sub>3</sub> and the conventional s-SrTiO<sub>3</sub>, Sr enrichment is most likely responsible for its

superior photocatalytic properties. These observations show that ion exchange reactions make it possible to synthesize structures and compositions not accessible by other means; in this case, the unique SrTiO<sub>3</sub> produced from BaTiO<sub>3</sub> is an improved hydrogen evolution catalyst.

### 4. Experimental Section

**Photocatalyst Synthesis:** All catalysts were prepared using a molten salt method. In a typical reaction, 0.3 g SrTiO<sub>3</sub> (Sigma-Aldrich, 99.9%) or BaTiO<sub>3</sub> (CERAC, 99.9%) was mixed with SrCl<sub>2</sub> (Alfa Aesar, 99.5%) at a molar ratio of 1:10 with an agate mortar. The mixture was then transferred to a covered alumina crucible (Sigma-Aldrich, Coors high-alumina, 50 mL) and annealed at 1150 °C for 10 h in air with a ramp rate of 10 °C min<sup>-1</sup>. Next, the mixture was centrifuged four times in deionized water and four times in ethanol to remove any residue of SrCl<sub>2</sub>. The powders collected through the centrifugation was dried in an oven at 80 °C over night.

RhCrO<sub>x</sub> cocatalysts were deposited (0.1 wt% Rh and 0.1 wt% Cr) on all samples with an impregnation method described elsewhere.<sup>[39]</sup> A total of 50 mg of as-prepared powdered samples was dispersed into 0.5 mL of deionized water containing appropriate amounts of Na<sub>3</sub>RhCl<sub>6</sub> (Sigma-Aldrich) and Cr(NO<sub>3</sub>)<sub>3</sub>·6H<sub>2</sub>O (Sigma-Aldrich, 99%) to yield 0.1 wt% Rh and Cr. The suspension was evaporated in a boiling water bath under constant manually stirring. The resulting powders were collected and heated at 350 °C for 1 h.

**Characterization:** The crystal phase was analyzed with an Empyrean X'pert PRO X-ray Diffractometer (PANalytical, Philips, Netherlands) in the range of 20–90° using a step size of 0.01°, equipped with a high-intensity (45 kV, 40 mA) Cu Kα radiation source (Kα1 = 1.5406 Å, Kα2 = 1.5444 Å). Scanning electron microscopy (SEM) images were obtained to determine the morphologies of all samples using a FEI Quanta 600 with a 30 kV accelerating beam and a spot size of 3. An Oxford full-analytical XMAX 80 mm SDD EDX detector was equipped on the SEM for chemical composition analysis (EDS). The particle cross-section samples were prepared using a focused ion beam (FIB) milling process with a gallium source on an FEI NOVA 600. TEM images were recorded with a FEI Tecnai F20 or a Thermal Fisher Themis 200 at 200 kV. X-ray photoelectron spectroscopy (XPS) spectra were conducted using a SPECS System with a PHOIBOS 150 Analyzer. N<sub>2</sub> adsorption–desorption measurements (Nova 2200e, Quanta-chrome, FL), used to determine the specific surface areas of powders through a Brunauer–Emmett–Teller (BET) approach, were performed at 77 K using a multipoint method. The sample was degassed at 120 °C for 24 h prior to measurement. UV–vis diffuse reflectance spectra were recorded on an OL 770 Multi-Channel

Spectroradiometer (Optronic Laboratories). ICP-OES was carried out at Element Technology to determine the Al<sup>3+</sup> concentration. X-ray fluorescence spectroscopy (XRF) was used to measure the concentration of Cl<sup>-</sup> in samples using an Oxford X-supreme 8000.

**High-Throughput Screening of Photocatalysts:** Photocatalytic hydrogen generation was measured with a high-throughput method using a Parallelized and Automated Photochemical Reactor (PAPCR), which enabled the authors to study up to 108 samples simultaneously.<sup>[20,22,40]</sup> The reactor array consisted of 108 glass vials with 10 mg catalyst powders added, and the illumination was provided by two high-power LED chips (Chanzon). The illumination wavelength of the LEDs was 380 nm. To explore the solution effect on the photocatalysts, 0.4 mL of DI water whose pH was adjusted to pH 2, 7, and 12 or 10% methanol solution with an unadjusted pH was injected into each vial. The headspace of the vials was covered by a layer of H<sub>2</sub>-sensitive film (DetecTape, Tape-Midsun Specialty Products) whose color would change from light to dark when exposed to H<sub>2</sub>. The calibration between the film darkness and local H<sub>2</sub> concentration had been extensively reported in the previous publication.<sup>[20]</sup> During a 16 h illumination, the H<sub>2</sub>-sensitive film was captured by a camera every 6 min and the pictures were used to calculate the rate of hydrogen production. A schematic of the reactor assembly was presented in Figure S1a (Supporting information).

**Apparent Quantum Yield Measurement:** To measure the apparent quantum yield (AQY), a gas-chromatography-based reactor setup was employed and a schematic was given (Figure S1b, Supporting Information). In a measurement, 200 mg of degassed catalyst powders, together with 20 mL DI water, was added into a 50-mL EPA glass vial with argon atmosphere inside. The vial was illuminated for 3 h by two LEDs with a peak wavelength at 380 nm. After illumination, the amount of hydrogen in the vial headspace was analyzed with a gas chromatography. The light intensity of the LEDs was measured with a photodiode. The resulting photon fluxes were integrated over the bottom area of the vial (4.9 cm<sup>2</sup>), with the irradiation of the photocatalyst estimated to be 5.6 × 10<sup>16</sup> photons s<sup>-1</sup>. The AQY was calculated according to the following equation:

$$\text{AQY} = \frac{\text{number of H}_2 \text{ molecules produced} \times 2}{\text{number of incident photons}} \times 100\% \quad (4)$$

## Supporting Information

Supporting Information is available from the Wiley Online Library or from the author.

## Acknowledgements

This work was supported by the National Science Foundation (under grant No. DMR 2016267), and the authors acknowledge the use of the Materials Characterization Facility at the Carnegie Mellon University supported by grant No. MCF-677785. S.B. and E.M.L. gratefully acknowledge the support through the National Science Foundation under grant No. CHE-2102460. The authors acknowledge Katrina Ramirez-Meyers and Dr. Jay Whitacre on XRF analysis. The authors acknowledge Dr. Chuanzhen Zhou on conducting XPS analysis at the Analytical Instrumentation Facility (AIF) at North Carolina State University, which is supported by the State of North Carolina and the National Science Foundation (award number ECCS-2025064). The AIF is a member of the North Carolina Research Triangle Nanotechnology Network (RTNN), a site in the National Nanotechnology Coordinated Infrastructure (NNCI).

## Conflict of Interest

The authors declare no conflict of interest.

## Data Availability Statement

The data that support the findings of this study are available from the corresponding author upon reasonable request.

## Keywords

ion exchange, molten salt, photocatalysis, SrTiO<sub>3</sub>

Received: December 15, 2022

Revised: January 11, 2023

Published online: March 3, 2023

- [1] A. Fujishima, K. Honda, *Nature* **1972**, 238, 37.
- [2] Q. Wang, K. Domen, *Chem. Rev.* **2020**, 120, 919.
- [3] L. Spanhel, M. Haase, H. Weller, A. Henglein, *J. Am. Chem. Soc.* **1987**, 109, 5649.
- [4] S. Sato, J. M. White, *Chem. Phys. Lett.* **1980**, 72, 83.
- [5] T. Takata, K. Domen, *J. Phys. Chem. C* **2009**, 113, 19386.
- [6] J. Liu, Z. Wei, W. Shangguan, *ChemCatChem* **2019**, 11, 6177.
- [7] S. Bai, L. Wang, Z. Li, Y. Xiong, *Adv. Sci.* **2017**, 4, 1600216.
- [8] G. Liu, J. C. Yu, G. Q. (M.) Lu, H.-M. Cheng, *Chem. Commun.* **2011**, 47, 6763.
- [9] C. Ricca, U. Aschauer, *J. Chem. Phys.* **2022**, 156, 154703.
- [10] T. Teranishi, M. Sakamoto, *J. Phys. Chem. Lett.* **2013**, 4, 2867.
- [11] H. Tada, T. Mitsui, T. Kiyonaga, T. Akita, K. Tanaka, *Nat. Mater.* **2006**, 5, 782.
- [12] Q. Xu, L. Zhang, B. Cheng, J. Fan, J. Yu, *Chem* **2020**, 6, 1543.
- [13] L. Luo, S. Wang, H. Wang, C. Tian, B. Jiang, *Energy Technol.* **2021**, 9, 2000945.
- [14] E. Gabilondo, S. O'Donnell, R. Newell, R. Broughton, M. Mateus, J. L. Jones, P. A. Maggard, *Chem. – A Eur. J.* **2022**, 28, e202200479.
- [15] D. H. Kerridge, *Pure Appl. Chem.* **1975**, 41, 355.
- [16] W. Sundermeyer, *Angew. Chem., Int. Ed. Eng.* **1965**, 4, 222.
- [17] Y. Ham, T. Hisatomi, Y. Goto, Y. Moriya, Y. Sakata, A. Yamakata, J. Kubota, K. Domen, *J. Mater. Chem. A* **2016**, 4, 3027.
- [18] T. Takata, J. Jiang, Y. Sakata, M. Nakabayashi, N. Shibata, V. Nandal, K. Seki, T. Hisatomi, K. Domen, *Nature* **2020**, 581, 411.
- [19] A. Yamakata, H. Yeilin, M. Kawaguchi, T. Hisatomi, J. Kubota, Y. Sakata, K. Domen, *J. Photochem. Photobiol. A Chem.* **2015**, 313, 168.
- [20] M. Zhang, P. A. Salvador, G. S. Rohrer, *J. Am. Ceram. Soc.* **2022**, 105, 5336.
- [21] S. O'Donnell, C.-C. Chung, A. Carbone, R. Broughton, J. L. Jones, P. A. Maggard, *Chem. Mater.* **2020**, 32, 3054.
- [22] E. M. Lopato, E. A. Eikey, Z. C. Simon, S. Back, K. Tran, J. Lewis, J. F. Kowalewski, S. Yazdi, J. R. Kitchin, Z. W. Ulissi, J. E. Millstone, S. Bernhard, *ACS Catal.* **2020**, 10, 4244.
- [23] Z. Pan, R. Yanagi, Q. Wang, X. Shen, Q. Zhu, Y. Xue, J. A. Röhr, T. Hisatomi, K. Domen, S. Hu, *Energy Environ. Sci.* **2020**, 13, 162.
- [24] M. Zhang, P. A. Salvador, G. S. Rohrer, *ACS Appl. Mater. Interfaces* **2020**, 12, 23617.
- [25] A. C. Ianculescu, L. Mitoseriu, D. Berger, C. E. Ciomaga, D. Piazza, C. Galassi, *Phase Transitions* **2006**, 79, 375.
- [26] A. D. Smigelskas, *Trans. AIME* **1947**, 171, 130.
- [27] S. N. Ruddlesden, P. Popper, *Acta Crystallogr.* **1958**, 11, 54.
- [28] J. H. Haeni, C. D. Theis, D. G. Schlom, W. Tian, X. Q. Pan, H. Chang, I. Takeuchi, X.-D. Xiang, *Appl. Phys. Lett.* **2001**, 78, 3292.
- [29] M. Cardona, *Phys. Rev.* **1965**, 140, A651.
- [30] J. M. P. Martirez, S. Kim, E. H. Morales, B. T. Diroll, M. Cargnello, T. R. Gordon, C. B. Murray, D. A. Bonnell, A. M. Rappe, *J. Am. Chem. Soc.* **2015**, 137, 2939.

- [31] N. Domingo, E. Pach, K. Cordero-Edwards, V. Pérez-Dieste, C. Escudero, A. Verdaguier, *Phys. Chem. Chem. Phys.* **2019**, *21*, 4920.
- [32] K. Yamada, H. Suzuki, R. Abe, A. Saeki, *J. Phys. Chem. Lett.* **2019**, *10*, 1986.
- [33] H. Kato, Y. Sasaki, N. Shirakura, A. Kudo, *J. Mater. Chem. A* **2013**, *1*, 12327.
- [34] A. Vijay, K. Bairagi, S. Vaidya, *Mater. Adv.* **2022**, *3*, 5055.
- [35] D. I. Bilc, C. G. Floare, L. P. Zârbo, S. Garabagiu, S. Lemal, P. Ghosez, *J. Phys. Chem. C* **2016**, *120*, 25678.
- [36] J. Yang, X. Wu, Z. Mei, S. Zhou, Y. Su, G. Wang, *Adv. Sustain. Syst.* **2022**, *6*, 2200056.
- [37] Q. Wang, G. Wang, J. Wang, J. Li, K. Wang, S. Zhou, Y. Su, *Adv. Sustain. Syst.* **2022**, *7*, 2200027.
- [38] B. Neumann, C. Kröger, H. Jüttner, *Z. Elektrochem. Angew. Phys. Chem.* **1935**, *41*, 725.
- [39] K. Maeda, K. Teramura, H. Masuda, T. Takata, N. Saito, Y. Inoue, K. Domen, *J. Phys. Chem. B* **2006**, *110*, 13107.
- [40] W. Song, E. M. Lopato, S. Bernhard, P. A. Salvador, G. S. Rohrer, *Appl. Catal. B* **2020**, *269*, 118750.